Biosensors and Bioelectronics 208 (2022) 114190

Contents lists available at ScienceDirect

Biosensors and Bioelectronics

journal homepage: www.elsevier.com/locate/bios

Au@PtPd enhanced immunoassay with 3D printed smartphone device for quantification of diaminochlorotriazine (DACT), the major atrazine biomarker

Xiaofan Ruan [a], Victoria Hulubei [b], Yijia Wang [a], Qiurong Shi [a], Nan Cheng [a], Limin Wang [a], Zhaoyuan Lyu [a], William C. Davis [b], Jordan N. Smith [c], Yuehe Lin [a], Dan Du [a,*]

[a] School of Mechanical and Materials Engineering, Washington State University, Pullman, WA, 99164-2920, United States
[b] Department of Veterinary Microbiology and Pathology, Washington State University, Pullman, WA, 99164-7040, United States
[c] Exposure Science and Pathogen Biology, Pacific Northwest National Laboratory, Richland, WA, 99352, United States

ARTICLE INFO

Keywords:
Lateral flow immunoassay
Au@PtPd nanoparticle
Peroxidase-like activity
3D printing
Pesticide metabolite

ABSTRACT

Increased use of pesticides in agriculture requires new advanced techniques to monitor both environmental levels and human exposure of pesticides to avoid potential adverse health outcomes in sensitive populations. Atrazine is widely used to control broadleaf weeds, and here we developed a new sensor capable of detecting diaminochlorotriazine (DACT), the major metabolite and biomarker of atrazine exposure. We established an Au@PtPd nanoparticles labeled lateral flow immunoassay (LFIA) for immunochromatographic based rapid detection of urinary DACT. The detection was based on competitive immunoassay between the analyte and the BSA-conjugated antigen. As evaluated, the coupled mesoporous core-shell Au@PtPd nanoparticles, with superior peroxidase-like activity, as the signal indicator offers a rapid direct chromatographic readout inversely correlated with the concentration of analytes, providing a detection limit of 0.7 ng/mL for DACT. Moreover, the detection limits were boosted to as low as 11 pg/mL with the detectable range from 10 pg/ml to 10 ng/mL, through a one-step catalytic chromogenic reaction. A rapid readout device was developed by 3D printing to provide a stable real-time quantification of the color intensity capable of assessing both chromatographic and absorbance results. This Au@PtPd nanoparticle-based immunosensing platform, as well as the 3D printed readout device, provide a promising tool for on-site and ultrasensitive detection of pesticide biomarkers.

1. Introduction

Rapid expansion and industrialization of agriculture over recent decades has increased global food supplies to meet the demand of rapid population growth and reduced food shortages. However, increased pesticide use associated with this expansion has increased environmental pesticide burden and human exposure to pesticides (Tilman et al., 2001). Agricultural crop production relies on pesticides to control insects, weeds, and microbial populations and improve crop quality and quantity. Many pesticides are associated with adverse health effects in humans and other species (Nicolopoulou-Stamati et al., 2016). In order to manage this risk, advanced techniques to monitor both environmental levels and human exposure to pesticides are needed to reap the pest control benefits and avoid potential adverse health outcomes in sensitive populations.

Atrazine is one of the most widely used pesticides to control broadleaf weeds in crops. It is one of the primary pesticides detected in drinking water in the U.S (Gilliom et al., 2001). Although the safety of atrazine remains controversial, scientists have reported atrazine interferes with hypothalamic control of pituitary–ovarian function and induces mammary tumor production (Barr et al., 2007). Upon oral intake by humans, atrazine is rapidly absorbed and metabolically dealkylated forming deethyl-atrazine (DEA), deisopropylatrazine (DIA), and diaminochlorotriazine (DACT). Atrazine metabolites are eventually excreted mostly in urine within a week, primarily as DACT (Catenacci et al., 1993).

Due to their high efficiency and selectivity, immunosensing techniques have been widely used to detect biomarkers both in clinical and research settings. Antibodies recognize small molecules, proteins, or peptides as specific biomarkers (Zhang et al., 2017). Antibodies have

* Corresponding author.
E-mail address: annie.du@wsu.edu (D. Du).

https://doi.org/10.1016/j.bios.2022.114190
Received 24 January 2022; Received in revised form 9 March 2022; Accepted 12 March 2022
Available online 21 March 2022

been packaged into various kinds of immunosensing platforms for biomarker determination including electrochemical (Chikkaveeraiah et al., 2012; Felix and Angnes, 2018; Ruan et al., 2021), microfluidic (Sonker et al., 2017), Raman (Sonker et al., 2017), solution-based fluorescence (Li et al., 2010; Song et al., 2018), ELISA (Ambrosi et al., 2009; Ruan et al., 2019; Thiha and Ibrahim, 2015), and lateral flow immunoassay (LFIA) (Cheng et al., 2019; Wang et al., 2014; Yang et al., 2018) platforms. Among these options, LFIA or immunochromatographic test strip (ICTS) is the most commonly accepted form of biomarkers point-of-care testing (POCT) for its simple preparation and rapid determination. Classical gold nanoparticles (GNPs) based LFIA, produces an intense ruby red signal as a result of accumulation of GNPs probes on the limited space of the test line (Zeng et al., 2009). With the introduction of novel nanomaterials, LFIA became a more flexible and versatile platform for detection of antigens, as demonstrated by Li et al. who developed a quantum dot labeled LFIA for the rapid and sensitive detection of ceruloplasmin (Li et al., 2010). In more recent years, the nanozyme enhanced immunoassay has increased interest in the possibility of increasing the sensitivity of biosensors especially LFIA (Jiang et al., 2016; Kim et al., 2017; Niu et al., 2020). A recent study has shown that a ternary metal nanozyme has enhanced peroxidase-like activity compared with single noble metal nanoparticles and bimetal nanomaterials (Ding et al., 2018; Wu et al., 2019). Until now however, ternary metal nanozyme technology is just beginning to be used in LFIA for biosensing, taking advantage of the exceptional chromogenic and catalytic properties of ternary metal nanozymes.

LFIA quantitative measurements involve the use of bulky commercial test strip readers that require an electrical connection which limits their use in biomarkers POCT applications and onsite determinations. In the last ten years, the popularization of smartphone-based platforms opened a new technology for biosensing with cheap, portable imaging and detection devices (Hernández-Neuta et al., 2019; Li et al., 2016; Xu et al., 2015). For example, You et al. developed a smartphone-based cost effective, quantitative detection system for LFIA. The cellphone camera was used as the photodetector and LED flash as a light resource (You et al., 2013). Nan et al. established a smartphone-based analyzing software for two-dimensional Pt–Ni$(OH)_2$ nanosheet amplified LFIA for the sensitive rapid detection of pesticides. This application provided a fast analytical method for LFIA reading (Cheng et al., 2017). However, without a correct design and optical unit, the LFIA reading accuracy could be low for direct use of smartphones. However, 3D printing technology has provided a method for making small compact devices that make reading of LFIA more accurate and flexible (Ruan et al., 2020). The accuracy for reading LFIA devices could be improved by incorporating some of the technologies mentioned above. For example, Zhao et al. developed a 3D printed smartphone based on ambient light-sensing for a mesoporous core-shell Pd@PtNPs nanozyme-based transparent ICTS for enzymatic inhibition and phosphorylation detection, with improved sensitivity and accuracy (Zhao et al., 2018). However, these types of platforms could only be used for reading LFIA with a one channel output. For further improvement, there has been a need to develop a dual-functional optical platform for nanozyme based LFIA for both test strip chromogenic reading and catalytic absorbance reading with higher sensitivity and accuracy.

As reported here, we developed an Au@PtPd nanoparticle, i.e., nanozyme, labeled LFIA with a portable, low-cost 3D printed smartphone-based dual-functional optical platform (hereinafter referred to as DFOP). For the DACT lateral flow immunoassay construction, we compared three different Au@Pt_xPd_y nanozymes (Au@Pt_xPd_yNZs) for use as a signal reporter. We selected the Au@PtPdNZs for use as the signal reporter and conjugated it to a monoclonal antibody specific for DACT. In the presence of DACT, the Au@PtPdNZs labeled antibody binds to DACT. When the DACT concentration is low, a chromogenic signal is produced and shows up on the test line of the test strip. When the DACT concentration is high, the visual signal is reduced in intensity depending on the concentration of DACT present in the sample being tested. For the second step of the assay, the test strip is cut free and transferred to a well containing the TMB substrate system for the Au@PtPdNZs catalytic reaction. The sensitivity of the assay is increased through a catalytic amplification. Both the direct chromogenic signal on LFIA and the catalytic absorbance signal in wells are recorded by a 3D printed DFOP. The results are compared with results obtained with commercial test strip and microplate readers. The present study provides a novel and versatile analytical platform for rapid diagnosis of human exposure to pesticides. In addition, the use of Au@PtPdNZs as a great substitution of biological enzymes features advantages including robust activity, easy production, and relatively low cost.

2. Methods

2.1. Materials

Chloroauric acid ($HAuCl_4 \bullet 3H_2O$), sucrose, Tween-20, 3,3′,5,5′-tetramethylbenzidine (TMB) liquid substrate system for ELISA, bovine serum albumin (BSA), 2-chloro-4,6-diamino-1,3,5-triazine (DACT), potassium carbonate, sodium citrate, ascorbic acid, sodium hydroxide, phosphoric acid, hypoxanthine-aminopterin-thymidine (HAT) medium supplement (H0262-10VL), hypoxanthine thymidine (HT) medium supplement (H0137-10VL), and polyethylene glycol (PEG) fusion reagent (P7181) were purchased from Sigma-Aldrich Inc. (St. Louis, MO, USA). Chloroplatinic acid ($H_2PtCl_6 \cdot 6H_2O$), potassium hexachloropalladate (IV) (K_2PdCl_6), goat-anti-mouse IgG antibody, and RPMI 1640 cell culture medium supplemented with 10 mM HEPES, 13% calf serum, 50 μM 2-mercaptoethanol, penicillin/streptomycin, L-glutamine were obtained from Thermo Fisher Scientific Inc. (Waltham, MA, USA) Phosphate buffered saline (PBS, 0.01 M, pH 7.4) was purchased from Casson Labs Inc. (Smithfield, UT, USA). Human urine was purchased from Innovative Research Inc. (Novi, MI, USA) PBST was composed of PBS with 0.5% Tween-20. ICTS membrane films, glass fiber conjugate pad sheets and fiber absorbent pads were purchased from Millipore Sigma (Burlington, MA, USA). LFIA backing card was obtained from DCN Dx (Carlsbad, CA, USA). The 6-, 12-, and 96-well tissue culture plates were purchased form Genesee Scientific Co. (EI Cajon, CA, USA). The inhouse X63 AG8.653 (X63) myeloma-cell line fusion partner was used to develop the hybridoma producing the DACT monoclonal antibody.

2.2. Development of anti-DACT monoclonal antibody

Pacific Immunology Ramona CA was contracted to conjugate the DACT hapten to keyhole limpet hemocyanin (KLH) and BSA. The methods used to develop the DACT monoclonal antibody (mAb) are described in detail in Hamilton and Davis (1995). In brief, 5 BALB/c mice were hyperimmunized with 100 μg DACT-KLH at 2-week intervals for 5 months to increase the potential of developing a high affinity mAb. Sera were collected and tested for the presence of antibody using the ELISA. Three days after giving the mice a final boost of antigen, the spleens were collected and pooled. 10^8 spleen cells were used for fusion with the X63 AG8.653 (X63) fusion partner. The remainder of the spleen cells were cryopreserved for later use if needed. The spleen cells were washed in serum free RPMI and mixed with X63 at a ratio of 2.5/1 and centrifuged to form a pellet. The pellet was overlayed with one mL of PEG solution. The pellet was drawn into the PEG with a pipette and mixed for 30 s to disperse the mixture of cells into small aggregates. The mixture was then diluted into 10 mL of serum free medium to prevent further adherence of X63 cells with spleen cells. The cells were then centrifuged and resuspended in complete RPMI culture medium containing LPS mitogen stimulator and freshly prepared growth supporting thymocytes. The cells were spread into ten 96 well culture plates and cultured in a CO_2 incubator at 37 °C. At 24 h, HAT was added to stop DNA synthesis and replication of X63 cells not fused with a spleen cell. Supernatants from the cultures collected and tested for the presence of

antibody at 7 days using ELISA plates coated with DACT-BSA. Seventeen positive cultures were identified and transferred to 12 well culture plates to expand the cultures in RPMI medium containing HT to support growth of the hybridomas. The cultures were cryopreserved when they reached 75% fluency. Supernatants from the cultures were saved and used to test for affinity of the mAbs for DACT. Three cultures were selected for cloning and development of single cell clones. Monoclonal antibody from one cloned line proved to have an affinity high enough for use in development of the Au@PtPd enhanced immunoassay.

2.3. Device design and 3D printing of DFOP

The prototype of a 3D printed smartphone based DFOP device was designed in SolidWorks (CAD software) and manufactured through a fused deposition modeling 3D printer (End3Pro, Creality3D Co., Shenzhen, CHN). The DFOP integrates the dual quantification functions of test strip chromogenic result and 8-wells absorbance output, which relies on smartphone camera and image analysis software to achieve intelligent optical inspection. The main components of the DFOP include a light source enclosure, an 8-well strip adapter, an ICTS adapter, and an optical cassette (Fig. 1A). The optical cassette and the adapter are designed to provide a stable and excellent imaging environment with the inside fully enclosed in LFIA working state. The chromogenic LFIA test strip is inserted into the LFIA adapter before detection. The 8-well strip is placed into the 8-well table for assembly. With the use of a smartphone flashlight and a 45-degree mirror, the light path is guided into the smartphone rear camera where images of the chromogenic LFIA, or the 8-well strip are captured. Light from the smartphone flash is reflected by the mirror into the optical cassette to the LFIA/8-well table and guided back to the smartphone rear camera through the reverse path. The camera location is fixed by the smartphone adapter, with its position accurately calculated to fit with the light path. The ICTS and the 8-well strip have two different accessories (modules) that can be selected and installed as needed (Fig. 1B and C), thus the DFOP can be assembled for dual function use. The assembled DFOP size is only 96 mm × 90 mm × 41 mm (Fig. 1D) with accessories costs less than 5 dollars.

2.4. Image capture and analysis

The smartphone APP, i.e., Colorimeter, was employed for image processing with direct RGB (red, green, blue) value outputs, through which the quantification of chromogenic signal was obtained. For LFIA strips, the corresponding RGB values of test lines were converted to grayscale values simply by: Grayscale = (R + G + B)/3, then the difference between background grayscale and the test line grayscale ($G\text{-}G_O$) was employed as the signal strength. As for the readout of the catalytic chromatic reaction in the wells, the signal strength was calculated from RGB values by: Intensity (yellow/%) = (1 - B/255 - K)/(1 - K), where K = 1 - max (R/255, G/255, B/255).

2.5. Principle of detection

The DACT-BSA antigen and the goat anti-mouse polyclonal secondary antibody were dispensed on the test line and control line, Au@PtPdNZs labeled anti-DACT mAb was preloaded on the conjugate pad (Fig. 2A). In the presence of DACT in running buffer, sample flows through the conjugate pad and reach the absorbent pad by capillary action. In this process, Au@PtPdNZs labeled anti-DACT mAb would bind

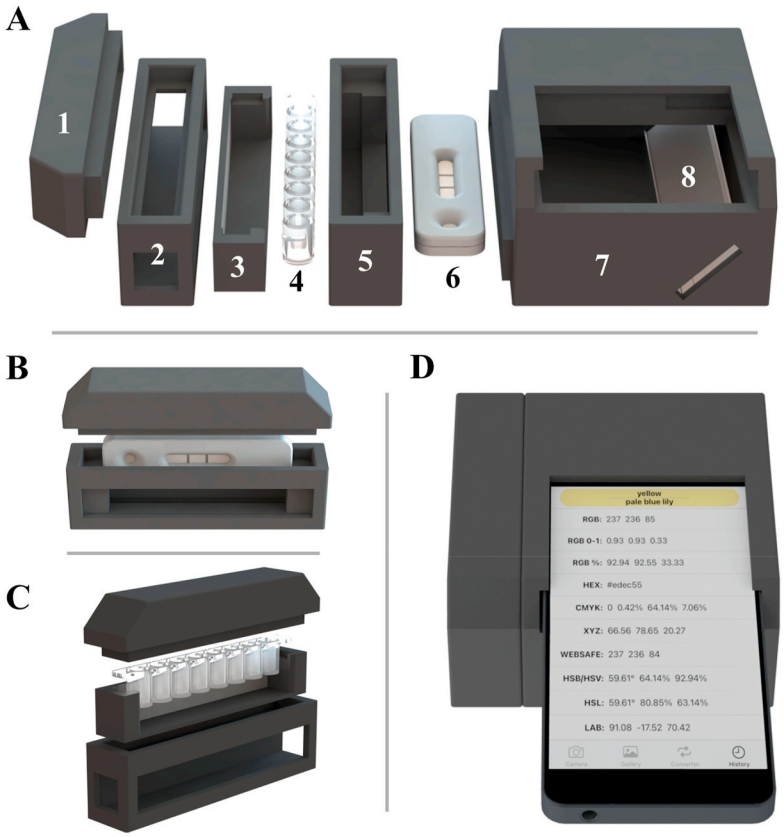

Fig. 1. 3D printed smartphone-based dual-functional optical platform. Expanded view (A): 1) light source enclosure, 2,3) 8-well strip adapter, 4) 8-well strip, 5) ICTS adapter, 6) ICTS, 7) optical cassette, 8) mirror. Assembled ICTS accessory (B) and 8-well strip accessory (C). Complete assembled device with integrated smartphone presenting an example of optical signal readout (D).

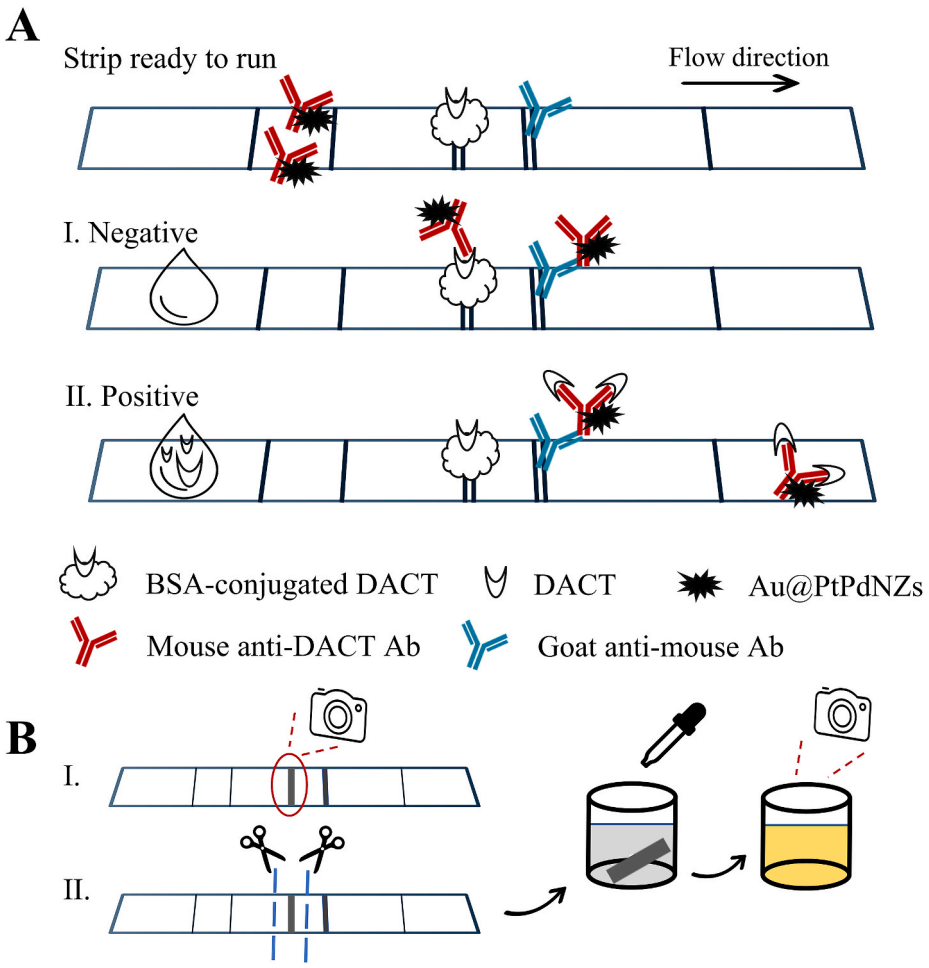

Fig. 2. Principle of ICTS detection: (A) Assembled ICTS with Au@PtPdNZ-Ab conjugates preloaded on the conjugate pad, BSA-conjugated DACT immobilized on the test line, and secondary antibody immobilized on the control line. Result in the absence of target (AI) and result in the presence of target (AII). Direct signal readout of ICTS result (BI) and catalytic enhanced readout (BII).

to DACT, resulting in the inhibition of binding to the DACT-BSA antigen immobilized on the test line. The passing anti-DACT mAb would eventually migrate to the control line and bind with the secondary antibody (Fig. 2AI). While in the absence of DACT in samples, the labeled anti-DACT mAb would bind to the DACT-BSA antigen, producing a strong signal on the test line. Excessive labeled anti-DACT mAb would conjugate with the secondary antibody on the control line (Fig. 2AII). Therefore, the signal strength on test lines represents the result of competition between DACT and the DACT-BSA antigen, inversely correlated to the level of DACT.

2.6. Preparation of Au@PtPdNZs

Au@Pt_xPd_yNZs were prepared according to the Shi et al. protocol with minor modification (Shi et al., 2016b). As a first step, 1.5 mL of 34 mM sodium citrate was added into a 100 mL clean glass reaction vial. Next, 0.5 mL of 25 mM $HAuCl_4$ was added into the first solution and mixed at room temperature. Afterwards, 0.5 mL of ultrapure water was added to bring the total volume of premixture to 2.5 mL and mixed. After 11 min incubation, a total volume of 12.5 mL of 5.0 mM H_2PtCl_6 and 5.0 mM K_2PdCl_6 solution were added to the above solution at a volume ratio of 1:0, 1:1, 0:1. After 30 min incubation at room temperature with mixing, 2 mL of 0.25 M ascorbic acid was added into the solution and incubated for 3 h. Finally, materials were centrifuged at 8, 000 rpm for 10 min using an Eppendorf 5417R centrifuge with an F-45-30-11 rotor, the supernatant was removed. After washing twice with acetone and three times with water, excess reaction precursor and reducing agent were removed from the solution. Au@PtNZs, Au@PtPdNZs, Au@PdNZs were obtained separately and stored at 4 °C before use. Freeze drying process was carried out to obtain powders for long term storage.

2.7. Preparation of Au@PtPdNZs-antibody conjugate

Au@PtPdNZs were combined with the anti-DACT mAb: 250 mM K_2CO_3 was added into 1 mL Au@PtPdNZs solution to adjust the pH to 8.2–8.3. Then, 5 μL of 2 mg/mL anti-DACT mAb was added into the above solution at room temperature for 60 min incubation to conjugate with Au@PtPdNZs. Afterwards, 100 μL of 10% BSA solution was added into the mixture and incubated for 30 min to block the excess binding sites. At the last step, the mixture was centrifuged at 10,000 rpm for 10 min in an Eppendorf 5417R centrifuge with an F-45-30-11 rotor, washed twice with 1% BSA in PBS buffer and dispensed in 100 μL of PBS containing 2% BSA and 3% sucrose.

2.8. Fabrication process of LFIA

The LFIA consisted of four parts integrated on a backing card, a sample pad, a conjugate pad, a nitrocellulose membrane, and an absorbent pad. First, the sample pad (17 mm × 30 cm glass fiber film) and the conjugate pad (9 mm × 30 cm glass fiber film) were placed in PBS buffer containing 2% BSA and 2% sucrose and air dried at room

temperature. The DACT-BSA antigen and goat anti-mouse polyclonal secondary antibody were dispensed on the test line and control line of nitrocellulose membrane (25 mm × 30 cm) separately with a dispensing system (XYZ3050, BioDot, Irvine, CA, USA). The distance between test line and control line was 8.0 mm. The nitrocellulose membrane was dried at 37 °C overnight and stored at 4 °C before use. The cotton absorbent pad was cut into 17 mm × 30 cm. Afterwards, the sample pad, conjugate pad, nitrocellulose membrane and absorbent pad were assembled on the LFIA back card in sequence with 2 mm overlapping. The assembled LFIA was compressed and cut into 4 mm wide test strips using an automatic cutting system (CM 4000, BioDot, Irvine, CA, USA). Finally, 2.5 μL of Au@PtPdNZs-antibody complex was precoated on each conjugate pad, the strips were dried overnight at room temperature and stored in a dry environment at room temperature for further use.

2.9. Assay procedure

Urine samples were first diluted (1:10) with PBS and spiked with different concentrations of DACT. The dilution of urine sample matrix has been considered through the experiments and calculations. The given concentration of spike samples represents the concentration in their original matrix, e.g., when 1 ppb of DACT was added to the 10-fold diluted urine standard, the concentration of DACT is 10 ppb in the original urine matrix. Then, 70 μL DACT sample was added onto the sample pad of LFIA strip, and samples migrated to the absorbent pad by the capillary action. After 10 min, dark signals appeared on the test line and the control line. The strip was then inserted into the strip slot for direct chromogenic test strip reading both on the 3D printed DFOP (Fig. 1B,D and Fig. 2BI) and the commercial test strip reader. For Au@PtPdNZs catalytic enhanced readout, the test line was cut out with a hole puncher and added into 150 μL TMB substrate system in wells for the catalytic reaction. After 10 min, the reaction was stopped by carefully removing test line and adding 100 μL of 0.1 M H_2SO_4 stop solution. The catalytic signals in wells were recorded by the 3D printed DFOP (Fig. 1C and D and Fig. 2BII) as well as the commercial microplate reader.

3. Results and discussion

3.1. Characterization of Au@PtPdNZs

The morphology of Au@PtPdNZs was investigated through scanning electron microscopy (SEM) with an FEI Quanta 200F instrument and transmission electron microscopy (TEM) with a Technai G2 20 Twin instrument with a 200 KV LaB6 electron source. As shown in Fig. 3, Au@PtNZs, Au@PtPdNZs, and Au@PdNZs particles presented similar spherical hyperbranched mesoporous nanostructure with outer layer of Pt and/or Pd and the inner core of gold. According to the particle size

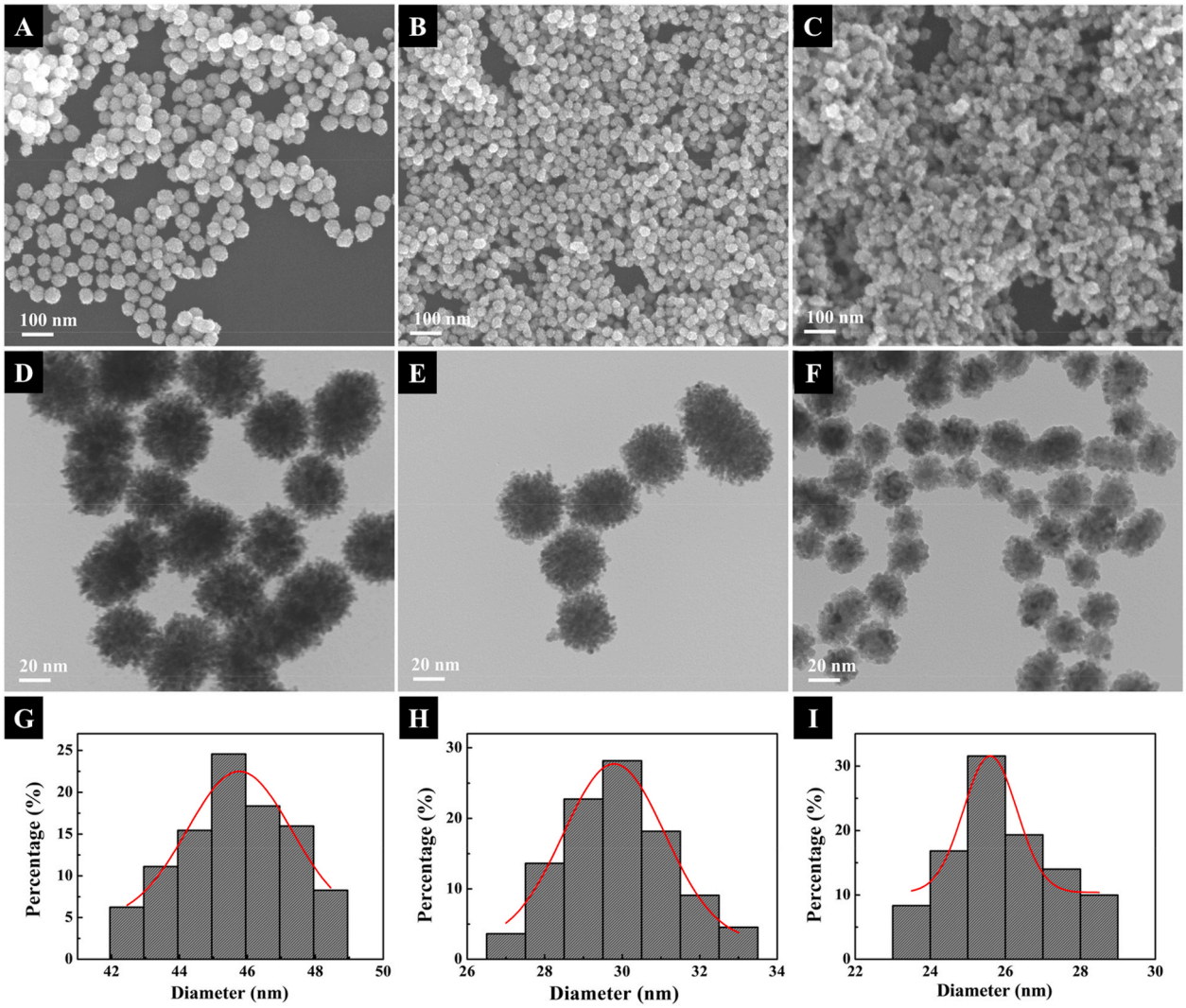

Fig. 3. SEM, TEM images and Dynamic light scattering (DLS) characterization of Au@PtNZs (A,D,G), Au@PtPdNZs (B,E,H), and Au@PdNZs (C,F,I).

distribution obtained from dynamic light scattering characterization (Fig. 3G–I), the average size distribution of Au@PtNZs, Au@PtPdNZs, and Au@PdNZs are 46 nm, 30 nm, and 26 nm, respectively. Through the synthesis, the Au core formed first as the reduction product by citrate via autocatalysis, then the Pt and/or Pd precursors were reduced after adding ascorbic acid, resulting the formation of the dendritic shell on the Au core. The mechanism of formation of the mesoporous dendritic core-shell structured Au@PtPdNZs has been systemically illustrated and reported in our previous work (Shi et al., 2016b). The mesoporous dendritic core-shell structure featured with enlarged surface area and enhanced mass transportation attributed to the geometric effect, offers exceptional catalytic performance. In addition, as the formation of the nanozymes employs a self-assembly gelation strategy that includes the formation of a core and the in-situ growth of a shell, the particle size is primarily determined by the reduction conditions, including the reaction time, ion types, and the ratio of metal precursors. Similar phenomena have been reported for the preparation of various nanoalloys such as the Pt/Pd, Pt/Au, Au/Ni, and Pt/Au/Ni nanoparticles (Ataee-Esfahani et al., 2013; Kannan et al., 2015; Sharma et al., 2019; Shi et al., 2016a). In this case, the particle sizes of the three substances Au@PtNZs, Au@PtPdNZs, and Au@PdNZs are the result of different reduction kinetics for different precursors.

The peroxidase-like catalytic activity of the synthesized nanoparticles were characterized and compared through catalyzed colorimetric reactions. In the presence of hydrogen peroxide, the peroxidase-mimic nanozymes induced the generation of active hydroxyl radicals, which oxidize the TMB and produces the blue oxidation product (Jiang et al., 2016; Niu et al., 2020; Ruan et al., 2021). As presented in Fig. 4A (a-d), 1 μL (1 mg/mL) of each Au@PtNZs, Au@PdNZs, and Au@PtPdNZs were added to 200 μL TMB substrate system and incubated for 1 min, among all tubes, the color of tube (d) (Au@PtPd) is the deepest, indicating the highest catalytic activity. The result is confirmed by measured absorbances shown in Fig. 4A. The superior activity of Au@PtPdNZs might be attributed to the trimetallic interaction, including the unique geometric and electronic effects, which provided favored Pt active sites for catalytic mediates. Thus Au@PtPdNZs was chosen to label the anti-DACT mAb.

3.2. Characterization of Au@PtPdNZs-antibody conjugate

The Au@PtPdNZs-antibody conjugate was characterized through zeta potential analysis. The conjugation relies on the passive absorption through electrostatic interaction between the negatively charged nanoparticles and positively charged amino groups of the antibody. As presented in Fig. 4B, the zeta potential of Au@PtPdNZs was −32.4 mV, indicating the negatively charged surface of Au@PtPdNZs before binding to the antibody. After the binding of anti-DACT mAb, the zeta potential was reduced to −15.7 mV. The change in zeta potential before and after binding confirmed that Au@PtPdNZs has been successfully bound to anti-DACT mAb.

3.3. Optimization of experimental conditions

Crucial experimental conditions of LFIA were optimized to ensure the analytical performance, such as treatment buffer of sample and conjugate pad, concentration of Au@PtPdNZs-antibody conjugate, and assay time. The treatment of sample and conjugate pad is significant for optimal delivery of samples and antibody complex. Proper treatment can reduce the nonspecific absorption to the membrane during flow of samples. For this purpose, BSA was mostly used as a blocking buffer of those unoccupied binding sites on sample and conjugate pad. Another important parameter is the running rate, which can be increased by adding Tween-20 to the treatment buffer or running buffer, to enhance the flowability of antibody immobilized particles. In addition, sucrose is generally used as an antibody stabilizer. Thus, to determine the optimal amount of BSA, Tween-20, and sucrose of the treatment buffer, a series of treatment buffers (a. PBS; b. PBST; c. PBS containing 2% BSA; d. PBST containing 2% BSA; e. PBS containing 2% BSA and 2% sucrose; f. PBST containing 2% sucrose; g. PBST containing 2% BSA and 2% sucrose; h. PBST containing 2% BSA and 3% sucrose; I. PBST containing 2% BSA and 4% sucrose.) were prepared for comparison. The signal ratio in the absence and presence (10 ng/mL) of DACT was employed to evaluate these buffers, while the amount of Au@PtPdNZs-antibody conjugate was kept at 2.5 μL and the assay time was 8 min. The sample pads and conjugate pads treated with different solutions were assembled on the test strips. Newly assembled test strips were used to detect 10 ng/mL DACT samples and the blank control, simultaneously. As shown Fig. 5A, the signal ratio of the LFIA shows the largest difference from the background intensity value when the sample pad and the conjugate pad were pretreated with PBS containing 2% BSA and 2% sucrose, Therefore, this treatment buffer was selected to pretreat sample pads and conjugate pads.

In addition, the amount of Au@PtPdNZs-antibody conjugate was optimized since the amount of the DACT-BSA antigen immobilized on test lines is fixed. For this purpose, the different amounts of conjugate (1.0 μL, 1.5 μL, 2.0 μL, 2.5 μL, and 3.0 μL) were applied on conjugate pads of strips. When the 2.5 μL Au@PtPdNZs-antibody conjugate was applied, the signal ratio of LFIA reached the highest value (Fig. 5B), thus, 2.5 μL the conjugate was employed in subsequent assays. In addition, the optimal incubation time for this LFIA was investigated. The signal intensity of LFIA gradually increases with the extension of the reaction time (Fig. 5C). When the reaction time reaches 8 min, the maximum

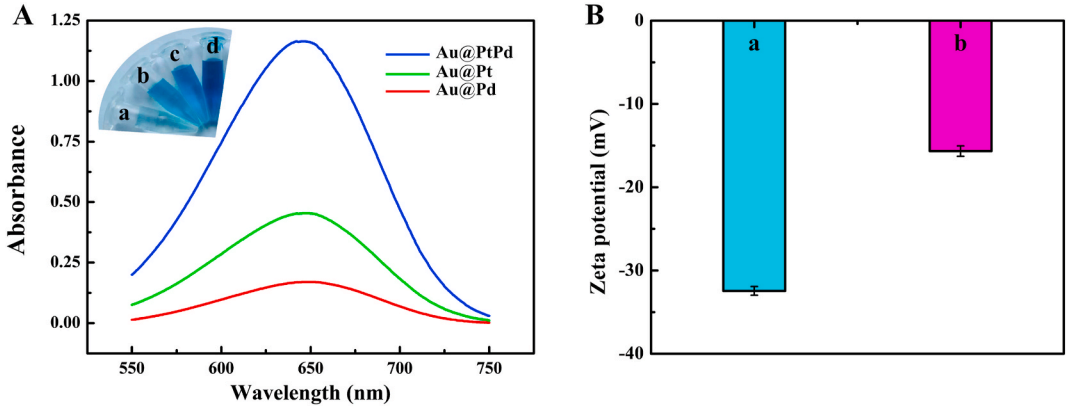

Fig. 4. (A) UV–vis spectrum of catalytic performance of Au@PtPdNZs in comparison with Au@PdNZs and Au@PtNZs. Visual result of 1 μL 1 mg/mL of each catalyst added to 200 μL TMB substrate system (Inset of A: a. TMB substrate system, b. Au@PdNZs, c. Au@PtNZs, d. Au@PtPdNZs). (B) Zeta potential of a) Au@PtPdNZs and b) Au@PtPdNZs-antibody complex.

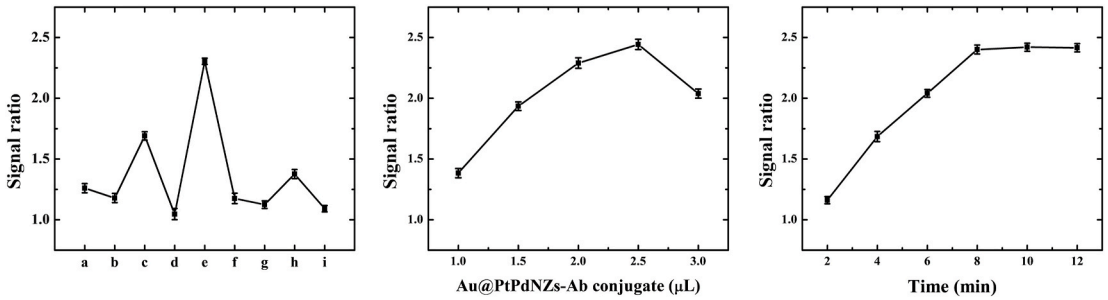

Fig. 5. Optimization LFIA conditions: (A) pretreatment of sample and conjugate pads using a) PBS, b) PBST, c) PBS with 2% BSA, d) PBST with 2% BSA, e) PBS with 2% BSA and 2% sucrose, f) PBST with 2% sucrose), g) PBST with 2% BSA and 2% sucrose, h) PBST with 2% BSA and 3% sucrose, i) PBST with 2% BSA and 4% sucrose; (B) amount of Au@PtPdNZs-Ab conjugate; and (C) assay time.

intensity was reached, indicating the saturated reaction was achieved. Thus, the optimal incubation time was determined as 8 min.

3.4. Performance of detection

Under optimal experimental conditions, we applied the LFIA-based sensing platform for DACT detection. 3D printed DFOP were used for direct chromogenic readout of strips and the subsequent catalytic chromogenic readout in wells. The visual signal was quantified by DFOP, and the direct chromogenic intensity of the test line on test strip demonstrated a good linear relationship with concentration of DACT (Fig. 6A). The logarithm of DACT concentration within the range from 0.5 ng/mL to 100 ng/mL with the algorithm regression equation of $y = 21.81*\log(x) + 19.98$ ($R^2 = 0.9937$), with a calculated detection limit of 0.7 ng/mL (based on 3*S/N). Moreover, taking advantage of the peroxidase-like catalytic ability of Au@PtPdNZs, the test lines of strips were cut out and placed into 150 μL of TMB substrate system (in wells) for 10 min, followed by adding of 100 μL 0.1 M H_2SO_4 as the stop solution. The chromogenic intensity of the wells was then analyzed by the DFOP. An enhanced detectable range from 10 pg/mL to 10 ng/mL was achieved with the algorithm regression of $y = 0.2896*\log(x) + 0.6128$ ($R^2 = 0.9948$) (Fig. 6B). The detection limit was boosted to as low as 11 pg/mL. To validate the reliability of the DFOP, the analytical accuracy was investigated in comparison with commercial strip reader and plate (absorbance) reader. With the increasing of Au@PtPdNZs concentration, the DFOP and commercial readers outputs increased correspondingly (Figs. S2A–B). The DFOP outputs for ICTS were in good linear agreement with the commercial test strip reader output with the correlation coefficient (R^2) of 0.996, and the DFOP outputs of wells were in good linear agreement with the commercial microplate reader output with the correlation coefficient (R^2) of 0.998. The good correlation revealed that the DFOP has comparable detection abilities to commercial test strip reader and commercial microplate reader. In addition, the reproducibility of the approach was evaluated by RSD assays for the detection of DACT at 1 ng/mL, 5 ng/mL and 10 ng/mL employing both functions of the DFOP. The average RSD was 10.2% and 8.4% respectively in the direct test strip determination and the catalytic enhanced determination, representing an acceptable reproducibility of the DFOP.

4. Conclusion

In summary, we designed a portable, easy-to-operate DFOP for DACT detection with Au@PtPdNZs labeled LFIA. Both direct test strip chromogenic signal and its catalytic chromogenic intensity in wells were recorded through our DFOP. With direct RGB readout of ICTS, a detectable range from 0.5 ng/mL to 100 ng/mL was achieved with the detection limit of 0.7 ng/mL. With Au@PtPdNZs catalytic amplified readout, a detectable range was achieved between 10 pg/mL and 10 ng/mL, with the detection limit as low as 11 pg/mL. The enhanced sensitivity was attributed to the outstanding peroxidase-like activity of the hyperbranched mesoporous core-shell structure of Au@PtPdNZs due to the geometric and electronic effects. Through comparison, the 3D printed DFOP integrated with LFIA has comparable detection capability as commercial instruments, with miniaturized size and enhanced portability for onsite applications. The rapid detection could be realized at diverse locations, which greatly saves the costs and improved the feasibility of analysis. Also, the miniaturized DFOP enables real-time monitoring and real-time transmission of DACT testing results to hospitals for disease diagnosis attributed to the coupled smartphone. In addition, the versatile biosensing platform can be easily customized for various detection environment, e.g., fluorescent analysis, when installed with a good excitation light source.

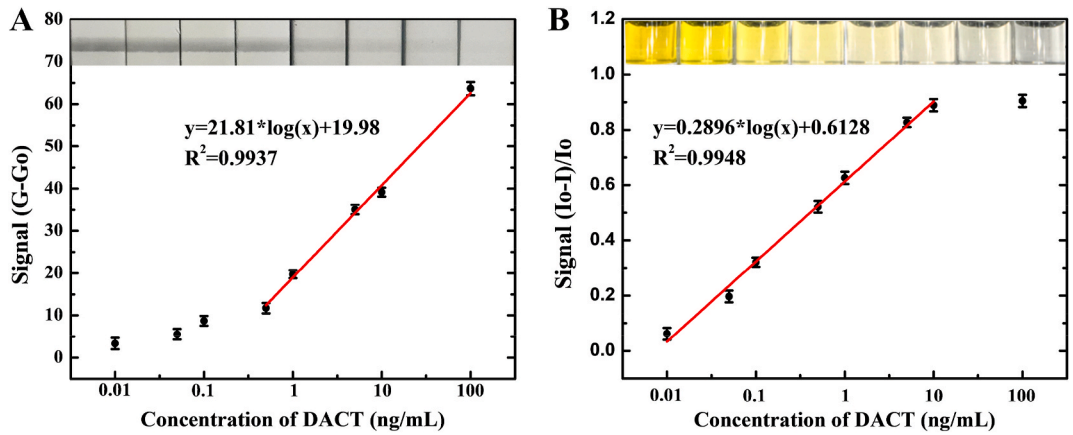

Fig. 6. Sensitivity of Au@PtPdNZs-amplified ICTS with dual module readout: (A) direct RGB-based determination of spike DACT concentrations from 0.01 ng/mL to 100 ng/mL; (B) catalytic enhanced determination of spike DACT concentrations from 0.01 ng/mL to 100 ng/mL.

Conflict of interest and authorship conformation form

Please check the following as appropriate:

All authors have participated in (a) conception and design, or analysis and interpretation of the data; (b) drafting the article or revising it critically for important intellectual content; and (c) approval of the final version.

This manuscript has not been submitted to, nor is under review at, another journal or other publishing venue.

The authors have no affiliation with any organization with a direct or indirect financial interest in the subject matter discussed in the manuscript.

CRediT authorship contribution statement

Xiaofan Ruan: Conceptualization, Methodology, Investigation, Formal analysis, Validation, Writing – original draft, Writing – review & editing. **Victoria Hulubei:** Resources, Investigation. **Yijia Wang:** Methodology, Investigation. **Qiurong Shi:** Resources. **Nan Cheng:** Methodology, Investigation. **Limin Wang:** Validation. **Zhaoyuan Lyu:** Resources, Formal analysis. **William C. Davis:** Resources, Writing – review & editing, Project administration. **Jordan N. Smith:** Writing – review & editing, Project administration. **Yuehe Lin:** Supervision, Writing – review & editing, Project administration, Funding acquisition. **Dan Du:** Conceptualization, Supervision, Project administration, Writing – review & editing, Funding acquisition.

Declaration of competing interest

The authors declare that they have no known competing financial interests or personal relationships that could have appeared to influence the work reported in this paper.

Acknowledgements

This work was supported by the Centers for Disease Control and Prevention/National Institute for Occupational Safety and Health, CDC/NIOSH) Grant No. R01OH011023-01A1. The opinions, findings, conclusions, or recommendations expressed in this paper are those of the authors alone, and do not necessarily reflect the views of CDC.

Appendix A. Supplementary data

Supplementary data to this article can be found online at https://doi.org/10.1016/j.bios.2022.114190.

References

Ambrosi, A., Airò, F., Merkoçi, A., 2009. Anal. Chem. 82, 1151–1156.
Ataee-Esfahani, H., Imura, M., Yamauchi, Yusuke, Yamauchi, Y., 2013. Angew. Chem. 125, 13856–13860.
Barr, D.B., Panuwet, P., Nguyen, J.V., Udunka, S., Needham, L.L., 2007. Environ. Health Perspect. 115, 1474–1478.
Catenacci, G., Barbieri, F., Bersani, M., Fereoli, A., Cottica, D., Maroni, M., 1993. Toxicol. Lett. 69, 217–222.
Cheng, N., Shi, Q., Zhu, C., Li, S., Lin, Y., Du, D., 2019. Biosens. Bioelectron. 142, 111498.
Cheng, N., Song, Y., Zeinhom, M.M.A., Chang, Y.-C., Sheng, L., Li, H., Du, D., Li, L., Zhu, M.-J., Luo, Y., Xu, W., Lin, Y., 2017. ACS Appl. Mater. Interfaces 9, 40671–40680.
Chikkaveeraiah, B.V., Bhirde, A.A., Morgan, N.Y., Eden, H.S., Chen, X., 2012. ACS Nano 6, 6546–6561.
Ding, Y., Yang, B., Liu, H., Liu, Z., Zhang, X., Zheng, X., Liu, Q., 2018. Sensor. Actuator. B Chem. 259, 775–783.
Felix, F.S., Angnes, L., 2018. Biosens. Bioelectron. 102, 470–478.
Gilliom, R.J., Barbash, J.E., Crawford, C.G., Hamilton, P.A., Martin, J.D., Nakagaki, N., Nowell, L.H., Scott, J.C., Stackelberg, P.E., Thelin, G.P., Wolock, D.M., 2001. Circular 1291, 1–184.
Hamilton, M.J., Davis, W.C., 1995. Methods Mol. Biol. 45, 17–28.
Hernández-Neuta, I., Neumann, F., Brightmeyer, J., Ba Tis, T., Madaboosi, N., Wei, Q., Ozcan, A., Nilsson, M., 2019. J. Intern. Med. 285, 19–39.
Jiang, T., Song, Y., Du, D., Liu, X., Lin, Y., 2016. ACS Sens. 1, 717–724.
Kannan, P., Yoon, C.S., Yi, S.C., Lee, S.Y., Kim, D.H., 2015. Mater. Chem. Phys. 156, 1–8.
Kim, M.S., Kweon, S.H., Cho, S., An, S.S.A., Kim, M. Il, Doh, J., Lee, J., 2017. ACS Appl. Mater. Interfaces 9, 35133–35140.
Li, F., Bao, Y., Wang, D., Wang, W., Niu, L., 2016. Sci. Bull. 61, 190–201.
Li, Z., Wang, Y., Wang, J., Tang, Z., Pounds, J.G., Lin, Y., 2010. Anal. Chem. 82, 7008–7014.
Nicolopoulou-Stamati, P., Maipas, S., Kotampasi, C., Stamatis, P., Hens, L., 2016. Front. Public Health 4, 148.
Niu, X., Cheng, N., Ruan, X., Du, D., Lin, Y., 2020. J. Electrochem. Soc. 167, 037508.
Ruan, X., Liu, D., Niu, X., Wang, Y., Simpson, C.D., Cheng, N., Du, D., Lin, Y., 2019. Anal. Chem. 91, 13847–13854.
Ruan, X., Wang, Y., Cheng, N., Niu, X., Chang, Y.C., Li, L., Du, D., Lin, Y., 2020. Adv. Mater. Technol. 5, 2000171.
Ruan, X., Wang, Y., Kwon, E.Y., Wang, L., Cheng, N., Niu, X., Ding, S., Van Wie, B.J., Lin, Y., Du, D., 2021. Biosens. Bioelectron. 184, 113238.
Sharma, G., Kumar, A., Sharma, S., Naushad, M., Prakash Dwivedi, R., ALOthman, Z.A., Mola, G.T., 2019. J. King Saud Univ. Sci. 31, 257–269.
Shi, Q., Zhu, C., Fu, S., Du, D., Lin, Y., 2016a. ACS Appl. Mater. Interfaces 8, 4739–4744.
Shi, Q., Zhu, C., Li, Y., Xia, H., Engelhard, M.H., Fu, S., Du, D., Lin, Y., 2016b. Chem. Mater. 28, 7928–7934.
Song, C.K., Oh, E., Kang, M.S., Shin, B.S., Han, S.Y., Jung, M., Lee, E.S., Yoon, S.Y., Sung, M.M., Ng, W.B., Cho, N.J., Lee, H., 2018. Anal. Chim. Acta 1027, 101–108.
Sonker, M., Sahore, V., Woolley, A.T., 2017. Anal. Chim. Acta 986, 1–11.
Thiha, A., Ibrahim, F., 2015. Sensors 15, 11431–11441.
Tilman, D., Fargione, J., Wolff, B., D'Antonio, C., Dobson, A., Howarth, R., Schindler, D., Schlesinger, W.H., Simberloff, D., Swackhamer, D., 2001. Science 292, 281–284.
Wang, Z., Zhi, D., Zhao, Y., Zhang, H., Wang, X., Ru, Y., Li, H., 2014. Int. J. Nanomed. 9, 1699–1707.
Wu, J., Wang, X., Wang, Q., Lou, Z., Li, S., Zhu, Y., Qin, L., Wei, H., 2019. Chem. Soc. Rev. 48, 1004–1076.
Xu, X., Akay, A., Wei, H., Wang, S., Pingguan-Murphy, B., Erlandsson, B.E., Li, X., Lee, W., Hu, J., Wang, L., Xu, F., 2015. Proc. IEEE 103, 236–247.
Yang, D., Ma, J., Xue, C., Wang, L., Wang, X., 2018. J. Pharm. Biomed. Anal. 159, 119–126.
You, D.J., Park, T.S., Yoon, J.Y., 2013. Biosens. Bioelectron. 40, 180–185.
Zeng, Q., Mao, X., Xu, H., Wang, S., Liu, G., 2009. Am. J. Biomed. Sci. 70–79.
Zhang, X., Zambrano, A., Lin, Z.T., Xing, Y., Rippy, J., Wu, T., 2017. Arch. Immunol. Ther. Exp. 65, 111–121.
Zhao, Y., Yang, M., Fu, Q., Ouyang, H., Wen, W., Song, Y., Zhu, C., Lin, Y., Du, D., 2018. Anal. Chem. 90, 7391–7398.